

# An ALMA archival study of the clump mass function in the Large Magellanic Cloud

Nathan Brunetti<sup>1\*</sup> and Christine D. Wilson<sup>1</sup>

<sup>1</sup>*Department of Physics and Astronomy, McMaster University, Hamilton, ON, L8S 4M1, Canada*

Accepted XXX. Received YYY; in original form ZZZ

## ABSTRACT

We present 1.3 and 3.2 mm continuum maps of three star forming regions in the Large Magellanic Cloud (LMC) observed with the Atacama Large Millimeter/Submillimeter Array (ALMA). The data were taken as part of two projects retrieved from the ALMA public archive plus one project observed specifically for this work. We develop a technique to combine maps at these wavelengths to estimate dust-only emission corrected for free-free emission contamination. From these observations we identify 32 molecular clumps in the LMC and estimate their total mass from their dust emission to range from 205 to 5740  $M_{\odot}$ . We derive a cumulative clump mass function ( $N(\geq M) \propto M^{\alpha+1}$ ) and fit it with a double power law to find  $\alpha_{\text{low}} = -1.76_{-0.05}^{+0.04}$ ,  $\alpha_{\text{high}} = -3.3 \pm 0.2$ , and a break mass of  $2500_{-200}^{+300} M_{\odot}$ . A comparison to the 30 Doradus-10 mass function derived previously from CO (2-1) data reveals a consistent range of clump masses and good agreement between the fitted slopes. We also find that the low mass index of the LMC mass function agrees well with the high mass index for core and clump mass functions from several star forming regions in the Milky Way. This agreement may indicate an extension of the Milky Way power law to higher masses than previously observed.

**Key words:** stars: formation – ISM: clouds – galaxies: individual: LMC

## 1 INTRODUCTION

Millimeter observations beyond the Milky Way are beginning to probe the scales of clustered and individual star forming regions known as molecular gas clumps and cores. While filamentary structure has previously been shown to be ubiquitous in Galactic star forming molecular gas (André et al. 2010; Arzoumanian et al. 2011; Könyves et al. 2015) and in other galaxies (the Large Magellanic Cloud in carbon monoxide (CO): Fukui et al. 2008; Wong et al. 2011), it is the higher density clumps and cores within the filaments that directly set the initial conditions for the formation of stars and clusters.

The term “clump” is commonly used to refer to molecular gas structures observed with sizes from  $\sim 1$  to 10 pc and masses up to around  $10^4 M_{\odot}$  (Fujii et al. 2014) that can go on to form zero to many stars. They are commonly seen as bridging the gap between giant molecular clouds (GMCs) and cores, and are likely the sites of eventual clustered star formation (Lada et al. 1991a,b; Lada 1992). Molecular gas cores are typically defined as small ( $\lesssim 0.1$  pc,  $\lesssim 200 M_{\odot}$ ) overdensities where it is expected only one or several stars will

soon form (Reid & Wilson 2006b). Studies of star forming clouds have measured the mass functions of cores and clumps to relate populations of these objects to their local environments and compare to the populations of newly formed stars. The differential mass function is typically characterized by a power law written as

$$\frac{dN}{dM} \propto M^{\alpha} \quad (1)$$

(Netterfield et al. 2009; Könyves et al. 2015; Freeman et al. 2017) where  $\alpha = -2.35$  is the Salpeter (1955) stellar initial mass function (IMF) slope. The mass function can also be expressed in cumulative form and through integrating Equation 1 is fit by a single power law of the form

$$N(\geq M) \propto M^{\alpha+1}. \quad (2)$$

Other commonly-used functions include a piece-wise double power law (Johnstone et al. 2001; Motte et al. 2001; Reid & Wilson 2005, 2006a,b; Pattle et al. 2017), or a lognormal function

$$N(\geq M) \propto 1 - \text{erf} \left[ \frac{(\ln M - M_0)}{(\sqrt{2}\sigma)} \right] \quad (3)$$

(Reid & Wilson 2005, 2006a,b; Netterfield et al. 2009; Könyves et al. 2015). Galactic measurements of core and clump mass distributions have mostly resulted in power law

\* E-mail: brunett@mcmaster.ca

fits with indices between  $-1.25$  and  $-2$  but with some as steep as  $-3.2$  (Reid & Wilson 2006b; Netterfield et al. 2009; Könyves et al. 2015; Pattle et al. 2017). For simplicity, all power law indices in this paper are reported as  $\alpha$  from Equations 1 and 2.

These functional forms are motivated by the tendency for the mass functions to have a long tail at high masses combined with a flatter portion or turnover at low masses. Physically, the power law tail has been attributed to collapse in molecular clouds where gravity is dominating the motions (Ballesteros-Paredes et al. 2011), although it has been more directly shown to be occurring due to the appearance of strong density peaks in molecular clouds, however they arise (Tassis et al. 2010). Lognormal forms have been argued for as following from the density distribution of supersonic turbulence (Padoan et al. 1997), although the presence of supersonic turbulence is not necessary (Tassis et al. 2010). The combination of various independent stochastic processes impacting the distribution of molecular gas in clouds has been shown to lead to a lognormal distribution through the central limit theorem (Larson 1973; Adams & Fatuzzo 1996). However, observational evidence for the ubiquity of lognormal distributions may be more difficult to confirm than previously thought (Alves et al. 2017).

In addition to comparing mass distributions between different regions, core mass functions have also been compared to the similarly shaped stellar IMF. Chabrier (2003, 2005) showed the stellar IMF follows the original Salpeter (1955) power law index of  $-2.35 \pm 0.30$  above  $1 M_{\odot}$  with a lognormal turnover at low masses peaking around  $0.2 M_{\odot}$ . This mass distribution has been observed to be universal across environments such as the Galactic disk, young and globular star clusters, and the spheroid or stellar halo (Chabrier 2003, 2005; Krumholz 2014). A similar power law slope has been predicted for both the stellar IMF and core mass functions (Chabrier & Hennebelle 2010; Guszejnov & Hopkins 2015). The observed similarity in slopes has led to the idea that there exists a star formation efficiency that is independent of mass acting to transform the core mass function to the IMF (Alves et al. 2007; André et al. 2010; Könyves et al. 2015).

At higher masses the comparison is between the mass distributions of entire star clusters and the clump mass functions within their natal GMCs (Lada 1992). Lada & Lada (2003) compiled a list of 76 young star clusters still embedded within a GMC and from this derived a cluster mass function with power law index of  $-2$  between  $\sim 50$  and  $1000 M_{\odot}$ . Fall & Chandar (2012) found the mass functions of star clusters from six different galaxies were all well fit by power laws with indices close to  $-1.9$ .

With the wealth of information gathered on the mass distributions of cores and clumps in the Milky Way, the next step is to extend these studies to other galaxies. This provides new physical environments to test models against as well as larger samples from which to draw statistical conclusions. Two of our nearest neighbors, the Magellanic Clouds, are now well within reach of mm/sub-mm observations of molecular and dust emission for studies of the clump mass function. For example, Indebetouw et al. (2013) derived a CO mass function of 103 clumps at  $0.46$  pc resolution in the Large Magellanic Cloud (LMC) with the Atacama Large Millimeter/Submillimeter Array (ALMA). While extending

beyond the Magellanic Clouds promises a further variety of environments and larger sample sizes, such studies push even the most advanced observatories to their limits. Rubio et al. (2015) reported on 10 CO clouds in the Wolf-Lundmark-Melotte (WLM) galaxy with masses of  $5900$  to  $7.3 \times 10^4 M_{\odot}$ . At a distance of  $1$  Mpc, they achieved  $\sim 5$  pc resolution with ALMA. More recently, Schrubba et al. (2017) observed NGC 6822 with ALMA reaching  $2$  pc resolution at a distance of  $470$  kpc.  $156$  CO clumps were extracted with masses of  $9$  to  $3500 M_{\odot}$ . Thus, if we wish to sample the full range of clump sizes and even start to probe molecular core scales, we are limited to the nearest Local Group members.

The LMC is the ideal next step in studying resolved star formation after our Galaxy, given its proximity ( $49.97 \pm 1.11$  kpc, Pietrzyński et al. 2013) and nearly face on orientation. It is also a significantly different system from the Milky Way in which to study how stars form, with a lower average metallicity of  $\sim 1/3 - 1/4 Z_{\odot}$  (Rolleston et al. 2002; Dufour 1984). Lower metal abundance results in smaller quantities of dust and thus less shielding for star forming regions from UV radiation. This means molecular gas reservoirs may be smaller in mass (Fukui et al. 1999, 2001), limiting the star forming fuel throughout the galaxy. Fewer metals also reduces the cooling through line emission which can change the energy balance in molecular clouds. Finally, the characteristic peak mass of the stellar IMF has been predicted to shift to higher masses for low metallicity (Bromm 2005, albeit for near-zero metallicity conditions).

In this paper, we calculate and analyze the dust-derived clump mass function in the LMC to facilitate comparison with mass functions of star forming regions in the Milky Way. In § 2 we summarize the observations from each ALMA project we used and we describe our continuum map-making process. In § 3 we describe our method of isolating the dust-only emission in each region, our clump identification procedure, and the steps we took to fit and characterize our final mass function. In § 4 we discuss our results from § 3 and place them into the broader context of the study of molecular clump mass functions. The paper is summarized in § 5. Maps of each field included in our mass function are presented in Appendix A as observed emission as well as decomposed into dust-only and free-free-only emission.

## 2 OBSERVATIONS AND DATA REDUCTION

### 2.1 Spatial and spectral setups

We retrieved six publicly available projects from the ALMA archive containing observations of seven fields in the LMC covering the star forming regions 30 Doradus-10 (30 Dor-10), N159W, N159E, N113, N166, GMC 225 and PCC 11546. In addition, we obtained new data in Cycle 4 towards 30 Dor-10 with the 7 m Atacama Compact Array (ACA). The projects were observed between 2011 December 31 and 2017 April 21 spanning Cycles 0, 1, 2 and 4.

For all but one region, multiple pointings were observed across each field in both bands to produce mosaic maps. Mosaic pointings were roughly Nyquist-spaced in a given band to achieve relatively uniform coverage across the inner portion of the maps when imaged together.  $12$  m (main array) plus ACA data were obtained for all fields except N113,

**Table 1.** ALMA projects used in this paper.

Field Name	R.A. <sup>a</sup> (J2000)	Dec. <sup>a</sup> (J2000)	Project Code	Ref. <sup>b</sup>
30 Dor-10	05:38:48	-69:04:48	2011.0.00471.S	1
"	"	"	2016.1.01533.S	2
N159W	05:39:37	-69:45:48	2012.1.00554.S	3
N159E	05:40:09	-69:44:44	"	4
N113	05:13:18	-69:22:25	2013.1.01136.S	5
GMC 225	05:47:09	-70:40:16	2012.1.00603.S	6
"	"	"	2013.1.01091.S	"
N166	05:44:29	-69:25:43	2012.1.00603.S	"
"	"	"	2013.1.01091.S	"
PCC 11546	05:24:09	-71:53:37	2013.1.00832.S	7

<sup>a</sup> Phase center is given for multi-pointing mosaics or pointing center for single-pointing observations (N113).

<sup>b</sup> First publication using these data or observing PI name: (1) [Indebetouw et al. \(2013\)](#); (2) N. Brunetti; (3) [Fukui et al. \(2015\)](#); (4) [Saigo et al. \(2017\)](#); (5) C. Henkel; (6) A. Kawamura; (7) [Wong et al. \(2017\)](#).

which was observed as a single pointing and only with the main array. Numbers of pointings on a field and in a single band range from 1 (N113) to 170 (N166). Mapped areas cover between 0.21 square arcminutes (N113) and 7.5 square arcminutes (N166; refer to Table 3 for areas of each field in both bands).

To measure dust masses in molecular clumps we focused on continuum observations from 86 GHz to 100 GHz ( $\sim 3.2$  mm) and 217 GHz to 233 GHz ( $\sim 1.3$  mm) in ALMA's Bands 3 and 6, respectively. Observations at these frequencies likely also contain significant emission from sources other than thermal dust such as free-free emission. Effective bandwidths used in making the continuum maps ranged between 1.6 GHz and 4 GHz. The locations of the regions analyzed here are marked on the infrared image of the LMC in Fig. 1 and a summary of the observational details is given in Table 1.

## 2.2 Background on individual fields

The Tarantula Nebula, or 30 Doradus, is one of the most actively star forming regions in the LMC. It harbors the R136 star cluster which boasts stellar densities between  $10^4$  and  $10^7$   $M_{\odot} \text{pc}^{-3}$  ([Selman & Melnick 2013](#)). Multiple generations of star formation have occurred in 30 Doradus over the course of  $\sim 20$  Myr ([De Marchi et al. 2011](#); [Walborn & Blades 1987](#)). 30 Doradus has been observed as part of several LMC-wide surveys targeting different emission sources. In CO, it has been observed with NANTEN in  $^{12}\text{CO}$  (1-0) ([Fukui et al. 2008](#)) and with MOPRA in  $^{12}\text{CO}$  and  $^{13}\text{CO}$  (1-0) ([Hughes et al. 2010](#); [Wong et al. 2011](#)). The HERITAGE Key Project survey ([Meixner et al. 2013](#)) observed it in dust emission along with the rest of the LMC.

The GMC 30 Dor-10 ([Johansson et al. 1998](#)) is part of the Tarantula Nebula within 11 pc projected distance of R136. [Indebetouw et al. \(2013\)](#) observed 30 Dor-10 with ALMA in  $^{12}\text{CO}$  and  $^{13}\text{CO}$  (2-1) emission as well as 1.3 mm dust continuum at  $\sim 1.9''$  resolution. The dust map was used to derive a total  $\text{H}_2$  mass for the GMC of  $6 \pm 1 \times 10^4 M_{\odot}$ . Clumps identified in their  $^{12}\text{CO}$  and  $^{13}\text{CO}$  cubes were used to calculate individual  $\text{H}_2$  masses from both the dust and the CO data. [Indebetouw et al. \(2013\)](#) calculated a CO derived

mass function for their 103 clumps and fit it with a power law of  $\alpha = -1.9 \pm 0.2$ .

N159 was originally identified by [Henize \(1956\)](#) as an HII region and has since been extensively studied. Noted as the strongest CO intensity cloud in the initial NANTEN LMC survey ([Fukui et al. 2008](#)), N159 has been resolved into three major clumps N159W, N159E, and N159S ([Johansson et al. 1994](#)). Across the region, multi-line excitation analyses on  $\sim 10$  pc scales estimated molecular gas kinetic temperatures ranging from 10 to 25 K ([Heikkilä et al. 1999](#); [Bolatto et al. 2000](#)). ALMA observations of N159W suggest that its constituent group of compact HII regions may have formed through a cloud-cloud collision ([Fukui et al. 2015](#)). By adding a dynamical estimate of one of the young stellar objects (YSOs) of  $10^4$  yr, [Fukui et al. \(2015\)](#) showed that the collisional triggering of star formation likely occurred very recently. N159E contains multiple developed HII regions, the most prominent of which is the Papillon Nebula ([Mizuno et al. 2010](#)). [Saigo et al. \(2017\)](#) suggested a three cloud collision is occurring in N159E, with the Papillon Nebula protostar in the overlap region. They also observe a molecular hole around the protostar filled with 98 GHz free-free emission indicating the protostar has recently begun disrupting the molecular cloud from which it formed. N159S does not exhibit any current star formation.

N113 was also identified by [Henize \(1956\)](#) as an HII region. As part of a sample of four molecular clouds (N159W, N113, N44BC, and N214DE) observed with the Swedish-ESO-Submillimetre-Telescope (SEST), it exhibited significantly lower gas-phase  $\text{C}^{18}\text{O}/\text{C}^{17}\text{O}$  abundances compared to molecular clouds in the Milky Way and the centers of starbursts, with a mean across clouds of  $1.6 \pm 0.3$  ([Heikkilä et al. 1998](#)). Subsequent observations have shown it to contain the most intense maser in the Magellanic Clouds ([Imai et al. 2013](#)), clumpy molecular gas currently forming stars ([Seale et al. 2012](#)), and a host of YSOs as identified by Herschel and Spitzer ([Ward et al. 2016](#)). N113 is related to three young stellar clusters (NGC 1874, NGC 1876, and NGC 1877; [Bica et al. 1992](#)). It also contains a rich assortment of molecular species ([Paron et al. 2014](#)).

N166 is yet another region originally identified by [Henize \(1956\)](#), and [Fukui et al. \(2008\)](#) identified it as only containing HII regions. Two molecular clouds were observed overlapping its position in the second NANTEN survey and a follow-up observation with ALMA targeted a position between those two NANTEN-observed clouds. N166 was also observed with Atacama Submillimetre Telescope Experiment (ASTE) in  $^{12}\text{CO}$  (3-2) revealing densities of  $10^2$  to  $10^3 \text{cm}^{-3}$  and kinetic temperatures between 25 and 150 K in a  $22''$  beam ([Paron et al. 2016](#)).

GMC 225 is one of 272 GMCs identified by [Fukui et al. \(2008\)](#) in the second NANTEN survey of the LMC in  $^{12}\text{CO}$  (1-0) and shows no sign of massive star formation ([Kawamura et al. 2009](#)). With a CO-derived total mass of  $10^6 M_{\odot}$  and radius of  $\sim 73$  pc it was observed as part of a follow up ALMA project. It is  $\sim 1500$  pc south of 30 Dor-10 and east of the molecular ridge.

PCC 11546 is an extremely cold ( $\lesssim 15$  K) dust source identified in the southern limits of the LMC as part of the Planck Galactic Cold Cloud catalog ([Planck Collaboration et al. 2016](#)). It also exhibits strong CO (1-0) emission in the Planck integrated CO map and the MAGMA LMC CO

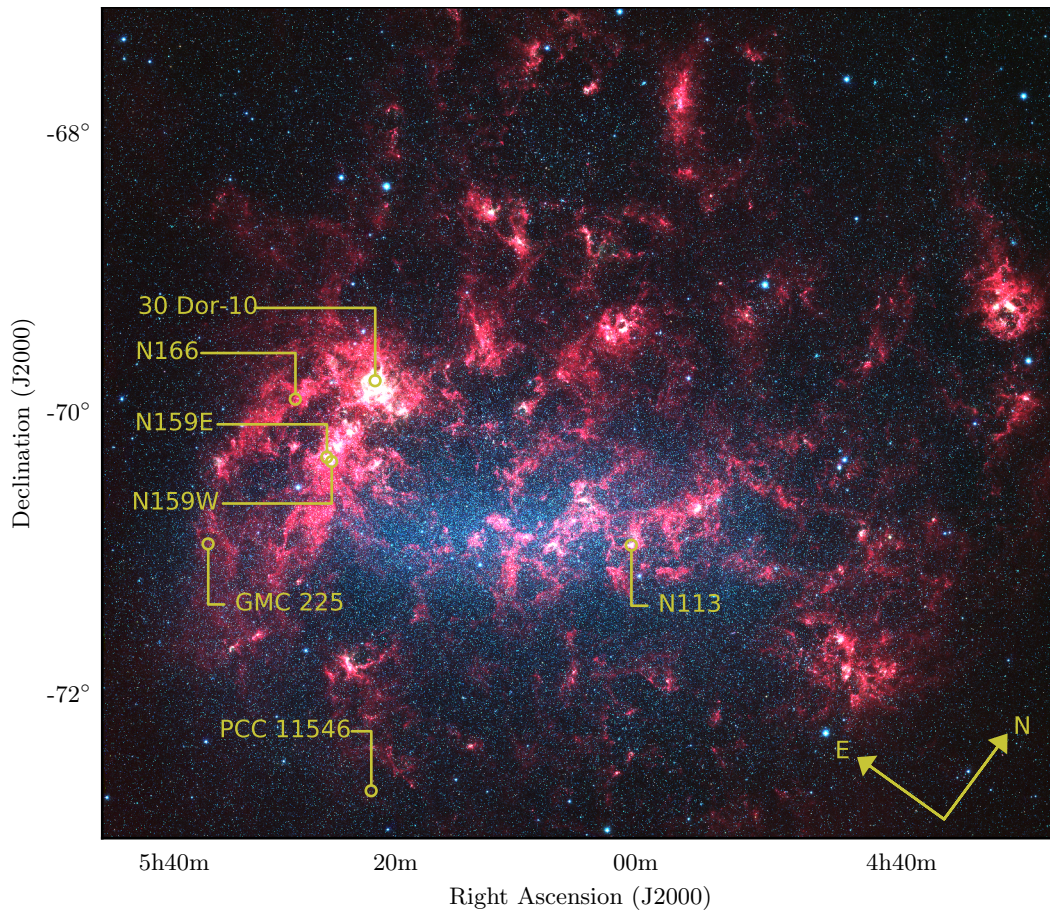


**Figure 1.** SAGE *Spitzer* IRAC three-color image of the LMC (Meixner et al. 2006). Red, green, and blue are 8, 4.5, and 3.6  $\mu\text{m}$ , respectively. The positions of the seven regions discussed in this paper are labeled.

survey (Wong et al. 2011). There appears to be a lack of massive star formation within PCC 11546 and it contains lower density gas than clouds closer to the center of the LMC (Wong et al. 2017).

### 2.3 Calibration

The visibility data were retrieved from the archive and calibrated. All fields except 30 Dor-10 had only raw data available in the archive. 30 Dor-10 had calibrated visibilities available and we used those data after recalculating the weights based upon the scatter in the visibilities using the Common Astronomy Software Applications (CASA) `statwt` command.

The observations with raw data available were either “manually” or pipeline calibrated at the observatory using CASA (McMullin et al. 2007). For manually calibrated data we ran the full calibration procedure using the observatory scripts in the latest version of CASA available at the time, 4.7.2-REL (r39762). Minor editing of the calibration scripts was necessary to account for task and parameter changes from the older versions of CASA. Edits were also made to ensure the visibility weights were properly calculated throughout the entire calibration procedure.

For pipeline calibrated data, we used the CASA and pipeline versions closest to those used by the observatory for

the original calibration<sup>1</sup>. There was no concern regarding visibility weights as all publicly available pipeline releases were after CASA 4.2.2 which contained a major correction to the handling of the weights.

Once calibrated data were obtained we inspected the visibilities from the calibrator sources to ensure the results of the calibration were as expected and all seriously problematic data were flagged. In most cases this inspection did not reveal anything that needed to be done beyond the observatory-provided calibration process. A few cases, however, did expose situations where marginal antennas or edge channels should have been flagged and we did so before imaging.

### 2.4 Imaging

All imaging steps, from inspecting the visibilities up to and including cleaning the maps, were carried out in CASA 4.7.2<sup>2</sup> (r39762) for all fields. Strong emission lines were iden-

<sup>1</sup> All versions of CASA were downloaded from [https://casa.nrao.edu/casa\\_obtaining.shtml](https://casa.nrao.edu/casa_obtaining.shtml).

<sup>2</sup> Note that after this paper was submitted, North American ALMA Science Center (NAASC) memo 117 was released detailing a problem with the flux scaling in 7 m ALMA mosaics imaged in versions of the CASA software prior to 5.0. We have measured the

tified with the `plotms` task and flagged before the visibilities were imaged to produce continuum maps. Since we combined maps in the two bands to create a dust-only emission map, we needed to match the spatial scales to which each pair of maps is sensitive as closely as possible. Matching the spatial scale sensitivities was achieved through a combination of trimming the shortest uv-spacings and tapering the weighting of the longest uv-spacings. To choose the “inner” uv trimming to use (the minimum uv-distance to include in imaging), we plotted the source visibility amplitudes versus their radial uv-distance in wavelengths for each band. The larger minimum baseline length of the two was used as the minimum uv-distance to include. For our fields, this minimum uv-distance was always set by the Band 6 data, so the uv-distance trimming was always applied to the Band 3 data.

The “outer” uv tapering directly changes the synthesized beam and sets the smallest spatial scale in the cleaned maps. The Band 6 maps always had smaller initial synthesized beams than the Band 3 maps. Once the uv-distance trimming was applied to the Band 3 data, we used the Band 3 synthesized beam as the target beam shape for the Band 6 uv tapering.

Matching the beam shapes precisely through tapering alone was not possible given the differences in intrinsic uv coverage between the observations. Therefore, we used the `restoringbeam` parameter in `clean` to force the Band 6 Gaussian beam shape to be the same as that of the Band 3 map. Note that this means all noise and any emission left in the residual maps is still at the tapered resolution and only the emission that was cleaned is exactly matched to the Band 3 resolution. However, we were always able to bring the beams into fairly close agreement with the uv-tapering. Differences between the Band 6 and Band 3 beam axes were <10 per cent (and usually much less) and position angle differences were <5 per cent. Only 30 Dor-10 had a larger position angle difference ( $\sim 30^\circ$  versus  $\sim 60^\circ$ ).

We cleaned all the dirty maps that showed obvious emission, which meant N166, GMC 225, and PCC 11546 were not cleaned. Motivated by the complexity of the emission in the 30 Dor-10 maps and by the desire to have a reproducible method of producing cleaned maps, we implemented an auto-masking algorithm for all cleaning. This algorithm is heavily based upon the auto-masking code given in the M100 CASA Guide as it appeared in August, 2016. We modified it to work as an automated CASA script<sup>3</sup>: when given a set of `clean` parameters, a minimum threshold to clean down to, a CASA region text file specifying an emission-free region of the dirty map, and a minimum spatial size to mask, the script iteratively cleaned down to the desired threshold. All auto-masking was done with stopping thresholds between 1.5 and 3 times the noise in the map and using minimum mask areas of 0.5 times the map synthesized beam. All fields

differences in clump fluxes between the 30 Dor-10 maps presented here and ones produced with CASA version 5.4.0-68 and find that on average, the Band 6 flux densities are overestimated by  $\sim 8$  per cent and Band 3 by  $\sim 2$  per cent. These small corrections have not been applied to the data presented in this paper.

<sup>3</sup> A full code listing of the auto-masking algorithm is available in Appendix B of Nathan Brunetti’s MSc thesis at <https://macsphere.mcmaster.ca/handle/11375/22656>.

were cleaned with Briggs weighting (Briggs 1995)<sup>4</sup>, with the `robust` parameter set to 0.5, in multi-frequency synthesis mode, with `psfmode` set to “psfclark” and using a maximum of  $10^4$  iterations. Table 2 lists the values used for important `clean` parameters for each field. The average synthesized beam size was  $\sim 2.3''$  corresponding to  $\sim 0.6$  pc at the distance to the LMC. Mapped areas cover between 44 (N113) and 1600 pc<sup>2</sup>.

## 2.5 Fields without detections

We tried to improve the signal-to-noise (S/N) in the maps with no continuum emission by setting `robust` to 2.0 to favor S/N over resolution. While the noise did drop, it was not enough to detect emission in any of the non-detection maps. The RMS noise and beam shapes listed in Table 3 for GMC 225, N166, and PCC 11546 refer to the maps made with `robust=2.0`.

Almost half of the fields we investigated were not detected in continuum emission. This raises the question of whether those data are inherently of poorer sensitivity compared to the data that has abundant emission. We tested this by matching the synthesized beams across all fields to the largest beam in each band. At 3.2 mm GMC 225 and N166 have the lowest root-mean-square (RMS) noise from our sample by a factor of 2-6. The 1.3 mm observations of PCC 11546 have a smaller RMS noise than the fields with detections and the sensitivities of GMC 225 and N166 at this wavelength are only a factor of 2-3 worse. This comparison suggests there are intrinsic differences in the physical densities and structures of the non-detection fields compared to the four detected regions.

## 3 DATA ANALYSIS

### 3.1 Free-free correction

Given the frequencies of these observations we expect the main contributions to continuum emission to be thermal emission from the  $\sim 30$  K dust and free-free emission from ionized gas. Although synchrotron emission is another possible source of continuum emission at these frequencies, HII regions, protostars, and young stars do not produce much synchrotron emission (Ginsburg et al. 2016). Colliding-wind binaries have been observed with spectral indices indicative of synchrotron radiation from particles accelerating in the wind collision zone (De Becker & Rauq 2013). However, following the method of Ginsburg et al. (2016), we estimate a 3.2 mm flux density of  $\sim 6 \mu\text{Jy}$  per binary. These flux densities are 30 to 100 times smaller than the noise in our fields (Table 3).

Fig. 2 compares the 1.3 and 3.2 mm fluxes for clumps identified in the 1.3 mm map. The solid line shows the flux scaling for free-free emission with exponent  $-0.1$  and two dashed lines show dust emission with exponents  $(2 + \beta)$  for  $\beta = 1$  and  $\beta = 2$ . Since the points are clustered between the free-free and dust scaling relations we conclude that there is

<sup>4</sup> Also see Dan Briggs’ PhD thesis at <http://www.aoc.nrao.edu/dissertations/dbriggs/> for the full details of the weighting scheme and for more information on the `robust` parameter.

**Table 2.** Important clean parameters used in imaging.

Field Name	cell <sup>a</sup> (")	imsize <sup>a</sup> (pixels)	threshold <sup>a</sup> (mJy/bm)	uvrange (> $\lambda$ )	minpb	robust	outertaper <sup>c</sup>		
							Major Axis (")	Minor Axis (")	Position Angle (°)
30 Dor-10	0.18	1152, 750	0.30, 0.78	5092	0.38	0.5	0.85	0.1	67
N159W	0.213	1000, 720	0.96, 1.32	8023	0.4	0.5	2.76	1.64	81
N159E	0.21	1250, 750	0.80, 1.78	5956	0.5	0.5	3.05	1.45	-70
N113	0.13	"	0.40	...	0.5	0.5	...	...	...
GMC 225	0.32, 0.11	700, 1500	...	...	0.5	2	...	...	...
N166	0.38, 0.155	1050, 1568	...	...	0.5	2	...	...	...
PCC 11546	0.126	1680 $\times$ 2400 <sup>b</sup>	...	...	0.5	2	...	...	...

NOTE.—Columns are named after clean task parameter names.

<sup>a</sup> For fields with two entries the Band 3 value is reported first and Band 6 second.

<sup>b</sup> Square maps were made for all fields except PCC 11546.

<sup>c</sup> Applied to the Band 6 data only.

**Table 3.** Image properties for each LMC field.

Field Name	Map Area <sup>a</sup>		Bandwidth <sup>b,c</sup> (GHz)	Synthesized Beam <sup>b</sup>			Noise <sup>d</sup>		
	Band 3 (Sq.')	Band 6 (Sq.')		Major (")	Minor (")	P. A. (°)	Dust	Band 3 (mJy/bm)	Band 6
30 Dor-10	1.9	1.2	4	2.25	1.40	65	0.41	0.15	0.39
N159W	1.9	1.6	1.9, 1.6	2.63	1.67	82	0.50	0.64	0.53
N159E	1.8	1.8	1.9, 1.6	2.90	1.61	-77	0.66	0.32	0.60
N113	...	0.21	2.5	1.35	1.04	61	...	...	0.26
GMC 225	4.0	3.4	1.9	4.26, 2.01	3.13, 1.13	-67, -86	...	0.18	0.76
N166	7.5	4.0	1.9	4.08, 2.17	3.57, 1.61	-73, 69	...	0.20	0.94
PCC 11546	...	5.8	3.4	1.81	1.23	75	...	...	0.19

NOTE.—Synthesized beam shape parameters are given for the final images used to create our clump mass function.

<sup>a</sup> Area of the mapped field above a gain response threshold of 0.5. Dust-only maps are only defined where both Band 3 and Band 6 data overlap so dust-only map areas are the same as the Band 6 maps. At the distance of the LMC, 1 square arcmin  $\approx$  212 pc<sup>2</sup>.

<sup>b</sup> For fields with two entries the Band 3 value is reported first and Band 6 second.

<sup>c</sup> Approximate bandwidth of continuum data used to produce the final maps. Bright emission lines are excluded in this estimate and in continuum imaging.

<sup>d</sup> Noise measurements were made in emission-free regions of the dirty map for each field.

significant free-free emission even at 1.3 mm. To use the dust emission to estimate the total mass of the clumps in these fields we need to correct for contamination from free-free emission at 1.3 mm.

If we assume that the dominant contributions are dust and free-free emission we can write

$$S_{B6} = S_d + S_{ff} \quad (4)$$

where  $S_{B6}$  is the Band 6 flux density,  $S_d$  is the dust-only flux density, and  $S_{ff}$  is the free-free-only flux density, all measured at 1.3 mm. For the Band 3 emission we can scale the dust and free-free emission from the Band 6 emission to obtain

$$S_{B3} = S_d \left( \frac{\nu_{B3}}{\nu_{B6}} \right)^{(2+\beta)} + S_{ff} \left( \frac{\nu_{B3}}{\nu_{B6}} \right)^{-0.1} \quad (5)$$

where  $S_{B3}$  is the Band 3 flux density,  $\nu_{B3}$  is the central frequency in Band 3,  $\nu_{B6}$  is the central frequency in Band 6, and  $\beta$  is the emissivity spectral index of the dust. While we expect the Band 6 and Band 3 emission to come mostly from dust and free-free emission sources, respectively, including terms for both in Equations 4 and 5 maintains the flexibility for the data to determine the relative fractions at each wavelength. The expression for the dust-only emission

at Band 6 from solving Equations 4 and 5 is then

$$S_d = S_{B6} - \frac{S_{B3} - S_{B6} \left( \frac{\nu_{B3}}{\nu_{B6}} \right)^{(2+\beta)}}{\left( \frac{\nu_{B3}}{\nu_{B6}} \right)^{-0.1} - \left( \frac{\nu_{B3}}{\nu_{B6}} \right)^{(2+\beta)}} \quad (6)$$

We combine the Band 3 and Band 6 images using Equation 6 to produce dust-only emission maps for our fields. We use an average value for the dust emissivity spectral index of  $\beta = 1.49$  from the [Gordon et al. \(2014\)](#) LMC-wide dust spectral energy distribution (SED) fits to Herschel observations. Specifically we use the broken emissivity modified blackbody (BEMBB) fit with unconstrained spectral index from [Gordon et al. \(2014\)](#). Dust-only maps for 30 Dor-10, N159W, and N159E are shown in Fig. 3.

We tested our algebraic decomposition using lower frequency radio observations that are often used to measure free-free and synchrotron emission directly. 4.8 GHz (6 cm) and 8.4 GHz (3 cm) observations were made of 30 Doradus ([Lazendic et al. 2003](#)) and N159 ([Indebetouw et al. 2004](#)) with the Australia Telescope Compact Array (ATCA). We applied spatial filtering to the radio images, to match the ACA uv coverage of the ALMA observations, through the CASA observation simulation functionality. This allowed us to better match the spatial scales measured at the differ-

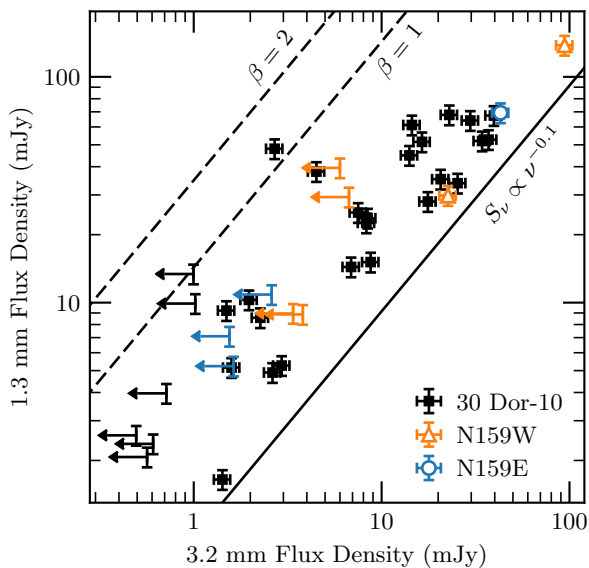


**Figure 2.** Comparison of 3.2 mm (Band 3) to 1.3 mm (Band 6) flux densities for clumps identified at 1.3 mm. Dashed lines show two different thermal dust emission scaling relations covering the range of realistic dust emissivity spectral indices, and the solid line shows a typical free-free scaling relation. Upper limits at 3.2 mm are for clumps found at 1.3 mm without significant co-spatial emission at 3.2 mm. Error bars correspond to 10 per cent calibration uncertainty.

ent frequencies (especially for 30 Dor-10 where the ACA uv coverage filtered out about 50 per cent of the radio flux).

We first measured total fluxes in each field at 4.8 GHz and 8.4 GHz. Adopting a synchrotron spectral index of  $-0.83$  and a free-free spectral index of  $-0.1$ , we iterated to estimate the balance of the two emission sources at the two frequencies. We then extrapolated the free-free component to the ALMA Band 3 frequency to get an estimate of the expected free-free emission at 3.2 mm.

To compare to this estimate, we solved for the free-free-only emission at Band 3 (see Appendix A for specific decomposition expressions and maps of free-free-only emission). Assuming a 10 per cent absolute flux calibration uncertainty on the radio continuum, the total free-free emission in 30 Dor-10 matches within 15 per cent between extrapolated and decomposed estimates (0.82 Jy and 0.97 Jy, respectively). N159W is consistent within the radio uncertainties, with 75 mJy and 78.5 mJy in the ATCA and ALMA maps, respectively.

N159E appears to have about four times too much free-free flux at Band 3 compared to the extrapolated flux (it has a near synchrotron-only spectral index in the radio maps). If the free-free emission becomes optically thick between 8.6 GHz and 98 GHz then the free-free spectrum would turn over (e.g. Turner et al. 1998) leaving just the synchrotron spectral index and a low free-free flux at low frequencies. Galactic ultracompact HII regions have been observed with free-free spectral turnovers at frequencies between 10 and 20 GHz (Wood & Churchwell 1989). It is possible that the main region of bright radio emission is originating from a population of ultracompact HII regions averaged together with supernova remnants within the ALMA beam leading to

synchrotron-dominated emission near 10 GHz and the presence of free-free emission at and above 100 GHz.

Lastly, we estimate that diffuse synchrotron emission contributes up to  $\sim 12$  per cent of the Band 3 flux. Since our method scales between Band 3 and 6 with the free-free spectral index this synchrotron component would be over-subtracted from the Band 6 flux by Equation 6. This results in, at most, four per cent of the total Band 6 flux being over-subtracted when making the dust-only maps by neglecting a synchrotron term in Equation 6. Considering the imperfect uv coverage matching between the ATCA and ALMA observations and the 10 per cent calibration uncertainty on the ALMA and ATCA observations, we believe the radio free-free emission estimates agree well enough and that the synchrotron is weak enough in Band 6 that we continue with our algebraic method.

We are not able to include N113 in our final mass function analysis because of the non-trivial free-free emission illustrated in Fig. 2 and our lack of observations at 3.2 mm for this field. Not being able to include N113 was unfortunate since it contributed about the same number of clumps in Band 6 as the N159E map, even within the much smaller area.

### 3.2 Clump finding

To identify molecular gas clumps in our dust-only maps we used the ClumpFind algorithm (Williams et al. 1994) available in Starlink<sup>5</sup> through the Cupid package (Berry et al. 2007). We chose to use this algorithm to facilitate direct comparison with previous work that also used ClumpFind. A total of 32 dust clumps were identified in three fields (30 Dor-10, N159W and N159E) with the majority found in 30 Dor-10. Clump properties are summarized in Table 4.

The RMS noise we input to ClumpFind was measured in each dust-only map from a region where no obvious emission, artifacts or negative bowls were visible. The lowest contour was set to three times the map RMS to ensure sources could be trusted with some confidence while also trying to recover most of the emission associated with a clump. Contour spacings were set to two times the RMS as this minimized splitting up sources while still recovering most of the obvious features. This combination of lowest contour level and contour spacing was also shown to result in the lowest number of missed and “false” clumps through synthetic source detection testing by Williams et al. (1994). Our own testing with several choices for these two settings showed that our final choice gave results that picked out distinct but somewhat blended sources without extracting spurious looking sources, along with staying well within believable bounds around obvious sources. Background subtraction was not used because the interferometer’s intrinsic spatial filtering removes large-scale emission, while the complicated interplay of bright emission can produce adjacent negative regions.

During completeness testing (§ 3.4) we found that our setting for the beam full width at half maximum (FWHM) parameter in ClumpFind caused the algorithm to reject

<sup>5</sup> The Starlink software (Currie et al. 2014) is currently supported by the East Asian Observatory.

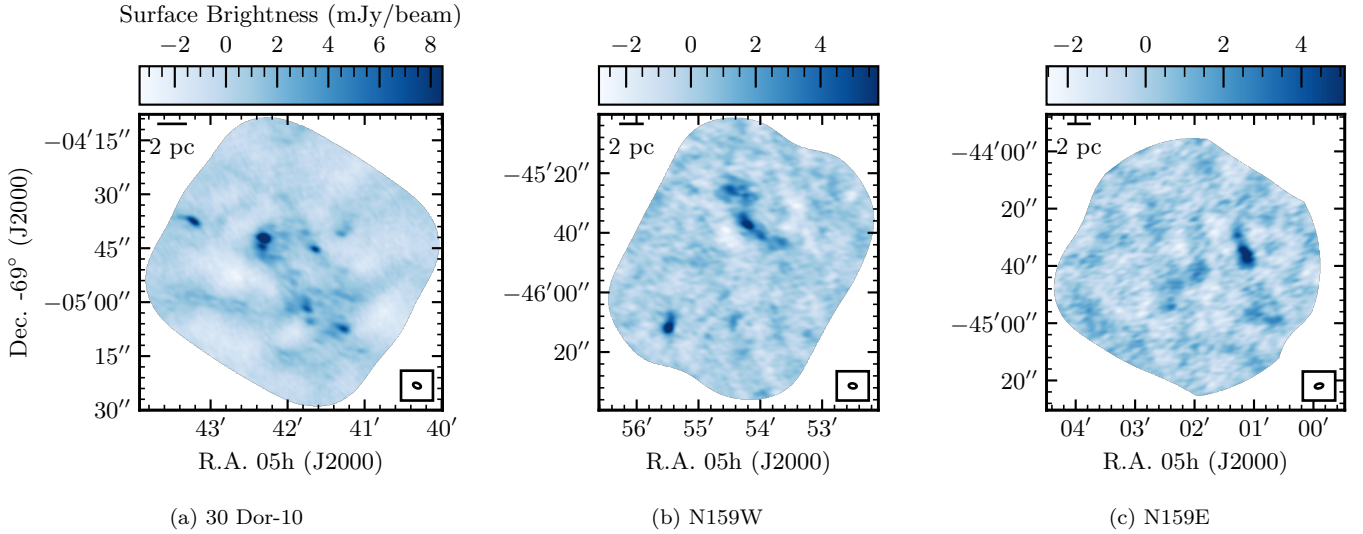


**Figure 3.** Dust-only maps of (a) 30 Dor-10, (b) N159W, and (c) N159E made from the combination of 3.2 mm and 1.3 mm ALMA observations. Contamination from free-free emission has been removed from these maps using Equation 6.

sources as too small when it should not have done so. To avoid this problem we instead set the FWHM parameter to zero and specified the `minpix` parameter to reject clumps that were too small. To determine the correct `minpix` value, we ran ClumpFind once with the FWHM set to the geometric mean of the synthesized beam axes and noted the `minpix` value ClumpFind calculated internally: 56 for 30 Dor-10 and N159W and 61 for N159E. This method gave the same resulting clumps as when using the FWHM parameter but it prevented clumps near the size of the beam from being rejected as too small due to the lowest contour setting (Berry, private communication). As this could select clumps that were of the same area as the synthesized beam but smaller than one of the beam dimensions (e.g. long and skinny clumps) we inspected the clump regions identified with ClumpFind visually for each field.

### 3.3 Converting dust flux to total gas mass

We calculated total mass (gas plus dust) for each of the clumps identified in our dust-only maps. Clump flux densities were converted to dust masses using

$$M_d = \frac{Sd^2}{\kappa B(T_d)} \quad (7)$$

where  $S$  is the dust flux density integrated over the spatial extent of the clump,  $d$  is the distance to the LMC,  $\kappa$  is the dust opacity per unit mass column density, and  $B(T_d)$  is the Planck function evaluated at the dust temperature  $T_d$ . Given the distance measurement from Pietrzyński et al. (2013) of  $49.97 \pm 1.11$  kpc we adopted a distance of 50 kpc for our calculations. The dust temperature and opacity were calculated from the Gordon et al. (2014) temperature and emissivity maps where we averaged the pixel values covering 30 Dor-10, N159W, N159E and N113 to obtain a temperature of 36.7 K and an opacity of  $1.16 \text{ cm}^2 \text{ g}^{-1}$ .

With the dust mass calculated using Equation 7 we applied a conversion to total gas mass through a gas-to-dust (G/D) ratio of 500 from Roman-Duval et al. (2017). This

G/D ratio was obtained by stacking the dust SEDs across the entire LMC as measured with IRAS and Planck in bins of varying gas surface density. Roman-Duval et al. (2017) derived atomic gas surface densities from 21 cm Parkes observations (Staveley-Smith et al. 2003) and molecular gas surface densities from  $^{12}\text{CO}$  (1-0) NANTEN observations (Mizuno et al. 2001). The stacked SEDs were fit with a modified blackbody to estimate the dust surface density, as well as the temperature and spectral emissivity index. We adopted the G/D from the highest gas surface density bin from Roman-Duval et al. (2017) as this is likely where stars are forming. Applying this conversion to our dust RMS noise measurements from Table 3 results in mass sensitivities ( $1\sigma$ ) of 45, 85, and  $72 M_\odot$  for 30 Dor-10, N159W, and N159E, respectively.

Fig. 4 shows the cumulative dust-only clump mass function along with the mass function derived from the 1.3 mm map assuming the 1.3 mm emission is purely from dust. Fig. 4 shows that our free-free correction is significantly larger than the random noise in each clump and systematically shifts the clump mass function to smaller masses.

### 3.4 Completeness corrections

We estimated the completeness of our mass function through Monte Carlo techniques by injecting synthetic sources of known fluxes and sizes into the dust-only maps one source at a time. We ran ClumpFind on the altered map with the same parameters as for the original maps and counted when synthetic clumps were recovered and when they were not. We then took the ratio of the number recovered to the total number injected as the completeness fraction. Synthetic source positions were randomly placed across the maps with a uniform distribution. All sources were elliptical Gaussians with FWHM and position angle identical to the synthesized beam for the corresponding map. We inject 600 synthetic sources per mass bin. Synthetic source masses were spaced evenly in log-space from roughly 21 to  $1.2 \times 10^4 M_\odot$ . Fig. 5 shows completeness data for 30 Dor-10, N159W and N159E.



**Table 4.** Properties of clumps in the LMC.

Name	R.A. <sup>a</sup> (J2000)	Dec. <sup>a</sup> (J2000)	Area <sup>b</sup> (pc <sup>2</sup> )	$S_{\text{ff,peak}}^{\text{c,d}}$ (mJy/beam)	$S_{\text{ff,int}}^{\text{c,e}}$ (mJy)	$S_{\text{d,peak}}^{\text{f,g}}$ (mJy/beam)	$S_{\text{d,int}}^{\text{f,h}}$ (mJy)	$M^{\text{i}}$ ( $M_{\odot}$ )
30 Dor-10 1	05:38:49.22	-69:04:42.24	2.6	3.7	21.5 ± 0.5	19.7	54 ± 2	5560 ± 160
30 Dor-10 2	05:38:52.84	-69:04:37.55	1.8	0.4	0.6 ± 0.4	9.5	27 ± 1	2750 ± 140
30 Dor-10 3	05:38:46.56	-69:04:45.30	1.5	0.9	-0.9 ± 0.4	8.3	18 ± 1	1890 ± 120
30 Dor-10 4	05:38:49.32	-69:04:44.40	3.4	1.9	6.2 ± 0.6	8.3	45 ± 2	4650 ± 180
30 Dor-10 5	05:38:45.08	-69:05:07.26	3.7	4.0	25.2 ± 0.6	7.5	44 ± 2	4530 ± 190
30 Dor-10 6	05:38:47.00	-69:05:01.68	4.9	1.4	5.4 ± 0.7	6.7	56 ± 2	5740 ± 220
30 Dor-10 7	05:38:46.83	-69:05:05.28	0.97	0.8	0.9 ± 0.3	4.2	9.8 ± 0.9	1012 ± 96
30 Dor-10 8	05:38:45.22	-69:04:40.98	1.2	0.6	-0.2 ± 0.3	3.8	11 ± 1	1110 ± 110
30 Dor-10 9	05:38:47.06	-69:04:40.80	1.4	2.7	6.6 ± 0.4	3.4	12 ± 1	1230 ± 120
30 Dor-10 10	05:38:48.21	-69:04:41.16	1.5	4.8	18.5 ± 0.4	3.1	13 ± 1	1330 ± 120
30 Dor-10 11	05:38:44.98	-69:04:58.26	3.1	1.0	7.1 ± 0.6	3.1	27 ± 2	2760 ± 170
30 Dor-10 12	05:38:47.70	-69:04:54.30	0.75	-0.3	-1.7 ± 0.3	2.7	6.3 ± 0.8	654 ± 85
30 Dor-10 13	05:38:46.39	-69:04:57.00	0.78	0.5	0.3 ± 0.3	2.6	6.8 ± 0.8	705 ± 87
30 Dor-10 14	05:38:44.21	-69:05:13.38	0.53	0.9	1.3 ± 0.2	2.6	4.1 ± 0.7	424 ± 72
30 Dor-10 15	05:38:52.14	-69:04:58.62	1.4	1.8	7.4 ± 0.4	2.5	10 ± 1	1070 ± 120
30 Dor-10 16	05:38:48.14	-69:05:14.10	1.5	1.2	2.7 ± 0.4	2.3	11 ± 1	1150 ± 120
30 Dor-10 17	05:38:47.60	-69:04:51.78	0.53	1.3	0.7 ± 0.2	2.3	4.3 ± 0.7	447 ± 71
30 Dor-10 18	05:38:50.29	-69:05:00.42	1.4	1.6	8.2 ± 0.4	2.2	10 ± 1	1060 ± 120
30 Dor-10 19	05:38:45.52	-69:04:59.70	0.64	1.0	1.3 ± 0.3	2.2	5.1 ± 0.8	524 ± 78
30 Dor-10 20	05:38:53.05	-69:04:57.53	1.6	2.9	12.4 ± 0.4	2.2	12 ± 1	1220 ± 130
30 Dor-10 21	05:38:46.36	-69:05:10.68	0.31	1.5	1.2 ± 0.2	2.1	2.4 ± 0.5	249 ± 55
30 Dor-10 22	05:38:45.96	-69:04:58.44	0.24	0.2	0.0 ± 0.2	2.1	2.0 ± 0.5	205 ± 48
N159W 1	05:39:41.90	-69:46:11.48	2.0	0.8	-1 ± 2	8.4	25 ± 2	2610 ± 230
N159W 2	05:39:36.77	-69:45:37.41	2.7	1.5	2 ± 2	7.6	31 ± 3	3200 ± 260
N159W 3	05:39:37.96	-69:45:25.27	3.3	21.8	54 ± 2	4.6	28 ± 3	2890 ± 290
N159W 4	05:39:35.95	-69:45:41.03	1.4	0.1	-1 ± 1	4.2	12 ± 2	1270 ± 190
N159W 5	05:39:36.93	-69:45:27.40	1.5	18.7	15 ± 2	4.0	13 ± 2	1290 ± 200
N159W 6	05:39:34.63	-69:45:42.94	1.5	0.3	-1 ± 1	3.3	11 ± 2	1150 ± 190
N159W 7	05:39:37.75	-69:46:09.57	0.73	5.5	6 ± 1	2.8	5 ± 1	530 ± 140
N159E 1	05:40:04.47	-69:44:35.88	1.8	11.3	26.9 ± 0.7	6.6	22 ± 2	2320 ± 180
N159E 2	05:40:04.71	-69:44:34.41	0.75	2.2	0.7 ± 0.5	6.0	9 ± 1	900 ± 120
N159E 3	05:40:05.08	-69:44:29.37	0.65	0.0	-0.4 ± 0.5	3.9	6 ± 1	570 ± 110

<sup>a</sup> Positions are peak positions as reported by ClumpFind.

<sup>b</sup> Calculated from the “square arcseconds” value reported by ClumpFind.

<sup>c</sup> Measured at 1.3 mm after correcting for dust contamination using Equation A1 to isolate for the free-free component.

<sup>d</sup> Uncertainties are random statistical uncertainties measured from each free-free-only map and are the same for all clumps in a given field: 0.2 mJy/beam for 30 Dor-10, 0.3 mJy/beam for N159W and 0.3 mJy/beam for N159E.

<sup>e</sup> Uncertainties are calculated by propagating uncertainties in each band through Equation A1. Uncertainties in each band are the RMS noise in each band times the square root of the number of beams covering the clump area in the free-free-only map.

<sup>f</sup> Measured at 1.3 mm after correcting for free-free contamination using Equation 6.

<sup>g</sup> Uncertainties are random statistical uncertainties measured from each dust-only map and are the same for all clumps in a given field: 0.4 mJy/beam for 30 Dor-10, 0.8 mJy/beam for N159W and 0.7 mJy/beam for N159E.

<sup>h</sup> Uncertainties are calculated by propagating uncertainties in each band through Equation 6. Uncertainties in each band are the RMS noise in each band times the square root of the number of beams covering the clump area in the dust-only map.

<sup>i</sup> Calculated using Equation 7 with  $T_{\text{d}} = 36.7\text{K}$ ,  $\kappa_{1.3\text{mm}} = 1.16\text{cm}^2\text{g}^{-1}$ , and  $G/D = 500$ .

We fit each completeness curve with a standard logistic function (Harris et al. 2016; Freeman et al. 2017)

$$f(M) = A \left\{ 1 + \exp \left[ -\alpha \left( \log_{10} \frac{M}{M_{\odot}} - M_0 \right) \right] \right\}^{-1} \quad (8)$$

where  $f(M)$  is the completeness fraction,  $A$  is an amplitude to allow for curves that do not asymptote to one,  $\alpha$  controls the width of the central part of the curve and  $M_0$  is the logarithm of the mass at which  $f = 0.5A$ . Fig. 5 shows the best fit curves and parameters for each field’s completeness data.

A surprising feature of the completeness curves shown in Fig. 5 is that none of the maps actually attain 100 per cent completeness. This is related to how crowded each map is: a

synthetic source added to a crowded map may land on a real clump so that ClumpFind does not find the extra clump. 30 Dor-10 is the most crowded map and has the lowest maximum completeness, while N159E is the least crowded and has nearly 100 per cent recovery at high masses. This trend shows that not only the noise and resolution but also the crowdedness of our maps are limiting our ability to find clumps.

It is important to note that we only tested source recovery for sources that were the same size as the synthesized beam, while most of the clumps we have identified are much larger than the synthesized beam. This is a general challenge in studying these types of objects, as molecular clumps are intrinsically amorphous in shape and vary sig-

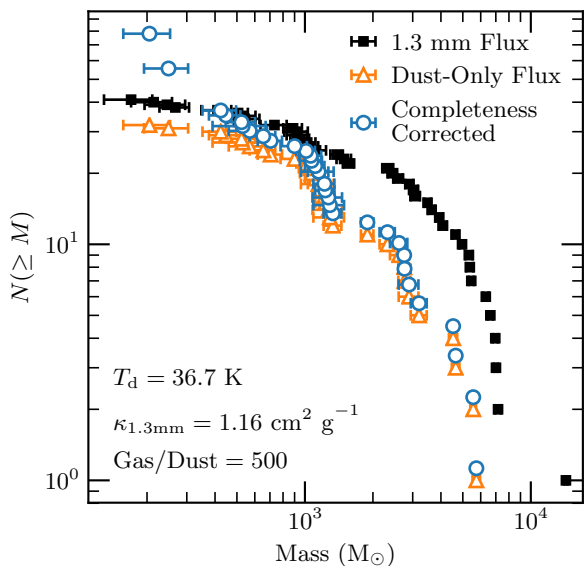


**Figure 4.** Comparison of cumulative clump mass functions from 1.3 mm maps (black squares), observed dust-only maps (orange triangles), and completeness corrected dust-only maps (blue circles). The parameters used to convert flux to gas mass in Equation 7 are shown in the bottom left. Error bars are random uncertainties on clump masses from noise in the maps; see § 3.3 for details.

nificantly in physical size. Since larger clumps of the same integrated flux density as smaller clumps have lower S/N, our completeness estimates are likely overestimating the total fraction of clumps recovered for a given mass. While more sophisticated methods can be employed (e.g. see Appendix B of Könyves et al. 2015) having a simplistic estimate of the completeness is better than no estimate.

We use the fits to the completeness data to correct the mass function numbers by calculating  $N_{\text{corr}} = N(\geq M)/f(M)$ . We used the 30 Dor-10 completeness curve because it contributes the majority of the clumps in our mass function. Applying this completeness correction produces the mass function shown as blue points in Fig. 4, in comparison to the observed mass function shown in orange points.

## 4 MASS FUNCTIONS IN THE LMC AND MILKY WAY

### 4.1 LMC clump mass function

An empirical mass distribution is typically plotted as either a differential mass function or a cumulative mass function. A differential mass function is calculated by defining mass bins spanning the mass range of objects and counting the number within each bin. This form allows for a simple Poissonian counting statistics approach to uncertainties for fitting but the results can depend on the choices of bin widths and centers. A cumulative mass function avoids complications from binning as it is just an ordered tally of masses at or above a given object’s mass. The trade off is that there is not a simple statistical approach to handling uncertainties for fitting.

A common model for the cumulative mass function of

clumps and cores is a broken power law with parameters for two independent power law indices and a break mass. This model can be written as

$$N(\geq M) = \begin{cases} AM_{\text{break}}^{(\alpha_{\text{high}} - \alpha_{\text{low}})} M^{(\alpha_{\text{low}} + 1)} & M < M_{\text{break}} \\ AM^{(\alpha_{\text{high}} + 1)} & M \geq M_{\text{break}} \end{cases} \quad (9)$$

where  $A$  is an arbitrary amplitude,  $M_{\text{break}}$  is the break mass where the power law index changes,  $\alpha_{\text{low}}$  is the power law index for masses below  $M_{\text{break}}$ , and  $\alpha_{\text{high}}$  is the power law index for masses above  $M_{\text{break}}$  (Reid & Wilson 2006b).

Given our relatively small sample of clumps and the simple model, we carried out our fits with the standard nonlinear Levenberg-Marquardt least-squares minimization (More 1977). To estimate fitting weights we followed the approach used by Reid & Wilson (2006a) which specifies the y-data uncertainties as the cumulative number  $N(\geq M)$  for each clump. The best fit double power law parameters are given in Table 5 for the mass function determined directly from the clump masses along with two variations that attempt to account for incompleteness. The procedure and inputs for the fits are the same across all three variations.

Given the form of the fitting function, there are only uncertainties in the x-values. To estimate the absolute uncertainties on the best-fit parameters we used Monte Carlo simulation, as done by Reid & Wilson (2006a). This involved generating  $10^5$  artificial mass functions and fitting each in the same way as the observed mass function. The artificial mass functions were made by drawing normally distributed random deviates centered on each measured clump mass and with standard deviations equal to the measurement uncertainties on the masses from the dust-only maps. Each newly generated sample of 32 masses was then sorted into descending order to prepare for fitting. Not only does this Monte Carlo approach simplify estimating the fit parameter uncertainties but it also nicely includes the effects of neighboring masses swapping places in the sorted order due to their uncertainties. From the distributions of fit parameters we used the inner 68 per cent to obtain the  $1\sigma$  uncertainties on each fit parameter (Table 5).

Fig. 6 shows the completeness-corrected mass function with the best fit double power law (Table 5). We use all clumps in our sample in this fitting with our lowest mass of  $205 M_{\odot}$  at the 41 per cent complete level. We also tested restricting the fit to masses above  $500 M_{\odot}$  in the uncorrected mass function since this is roughly where the 30 Dor-10 completeness curve flattens out at maximum completeness. The best fit double power laws for the two methods end up being statistically indistinguishable based on our Monte Carlo uncertainty estimates (Table 5) so we focus our analysis on the completeness corrected mass function.

It may appear unusual that the numbers of high mass clumps need to be boosted by our completeness correction. An overlapping pair of sources (merged clumps) would be identified in the data as a more massive clump and thus not be entirely missed. We tested removing the completeness correction to the high mass clumps by stitching together two sigmoid curves (the fit shown in Fig. 5 and a curve with the same width parameter but amplitude of 1.0 and shifted slightly to higher masses) to create a smoothly varying sigmoid matching our measured completeness at low masses and asymptoting to 100 per cent complete at high masses.

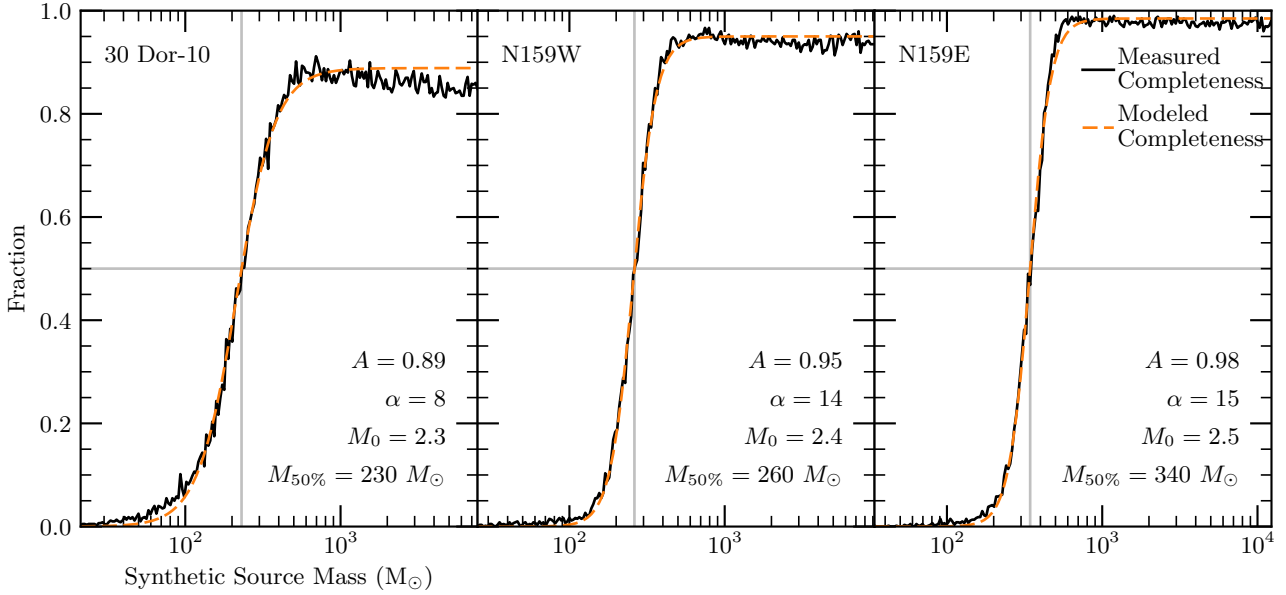


**Figure 5.** Completeness curves for point sources in 30 Dor-10, N159W, and N159E (black line). The best fit logistic curves (Equation 8) are shown as orange dashed lines with the best fit parameters in the bottom right. 50 per cent completeness is marked by the vertical gray lines and reported as  $M_{50\%}$  in the bottom right.

**Table 5.** Results of double power law and lognormal fits to cumulative clump mass function for the LMC.

	$\alpha_{\text{low}}$	$\alpha_{\text{high}}$	$M_{\text{break}}$	$M_0^{\text{a}}$	$\sigma$
Initial Guess	-1.8	-3.5	2500	7	1
Observed Mass Function	$-1.50^{+0.06}_{-0.05}$	$-3.3 \pm 0.2$	$2200 \pm 200$	$7.22^{+0.06}_{-0.04}$	$0.86^{+0.03}_{-0.04}$
Observed MF, $M > 500 M_{\odot}$ Only	$-1.74^{+0.01}_{-0.1}$	$-3.3 \pm 0.2$	$2500^{+300}_{-100}$	$7.3^{+0.2}_{-0.1}$	$0.81^{+0.04}_{-0.06}$
Completeness Corrected MF	$-1.76^{+0.04}_{-0.05}$	$-3.3 \pm 0.2$	$2500^{+300}_{-200}$	$6.8 \pm 0.2$	$1.03^{+0.06}_{-0.08}$

<sup>a</sup>  $\exp(M_0)$  is the central mass of the lognormal function from Equation 10. So, for example, the fitted central mass of the observed mass function is  $\exp(7.22) \approx 1370 M_{\odot}$ .

Refitting the mass function corrected with this piece-wise completeness curve did steepen both indices and moved the break to a higher mass but all within the uncertainties of our original fit.

For comparison with studies that fit mass distributions with a lognormal function we have also fit our completeness-corrected LMC mass function with

$$N(\geq M) = \frac{A}{2} \left[ 1 - \operatorname{erf} \left( \frac{\ln M - M_0}{\sqrt{2}\sigma} \right) \right] \quad (10)$$

where  $A$  is an arbitrary amplitude,  $\exp(M_0)$  is the central mass, and  $\sigma$  is a width parameter. Best-fit parameters are summarized in Table 5 along with  $1\sigma$  uncertainties. All fitting and uncertainty estimation was carried out identically to the double power law procedure.

## 4.2 Comparison to other studies

The sample of 11 core/clump mass functions from 7 different star forming regions analyzed by Reid & Wilson (2006b)

is a useful one for comparing our LMC clump mass function to Milky Way mass functions. All mass functions were re-calculated from the original literature sources and fit with a double power law (Equation 9) homogeneously across all regions. While there are various differences in how those data were acquired and processed as well as how individual cores and clumps were identified, using the best fit parameters reported by Reid & Wilson (2006b) will remove any variability introduced in the fitting step. Fig. 7 compares the high and low mass slopes from Reid & Wilson (2006b) with our fit from § 4.1 for the LMC.

The LMC break mass is greater than the individual clump masses for all of the Milky Way objects except for W43 and RCW 106 (and greater than all Milky Way break masses which range from  $0.2 \pm 0.1$  to  $400 \pm 300 M_{\odot}$ ). As a result, it is probably more reasonable to compare the LMC low mass slope to the high mass slopes of the Galactic clouds. Fig. 7 shows high mass indices for  $\rho$  Oph at 850  $\mu\text{m}$ , NGC 7538 (measured at both 450 and 850  $\mu\text{m}$ ), and W43 are consistent with the low mass index for the LMC. All low mass

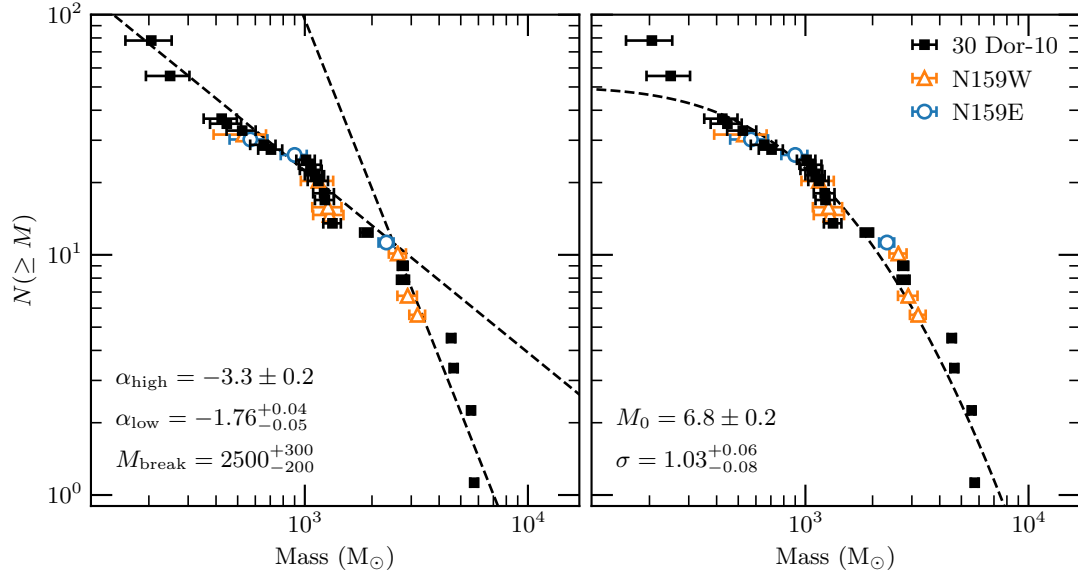


**Figure 6.** Completeness corrected clump mass function (points are the same as the blue circles in Fig. 4) with best fits plotted as black dashed lines; double power law on left and lognormal on right. Parameters of the fits (Equations 9 and 10) are shown in the bottom left. Clumps are color coded by the region from which they originate with 30 Dor-10 as black squares, N159W as orange triangles, and N159E as blue circles. Error bars are the same as in Fig. 4.

Galactic indices, except Orion B from [Motte et al. \(2001\)](#), are systematically shallower than the LMC low mass index. The observed consistency between the LMC low mass index and the high mass indices from  $\rho$  Oph, NGC 7538, and W43 suggests that the shape of the mass function may extend smoothly from the lower mass clumps of the Milky Way regions to the higher mass clumps of the LMC. In other words, it appears the mass function slopes at high masses in the Milky Way are extending up to the masses at the bottom of our LMC mass function.

In addition, none of the Galactic mass functions had completeness corrections applied and are all likely suffering from incompleteness at their low mass ends. Limiting our comparison to the high mass end of the Galactic mass functions, where incompleteness should have a minimal effect, gives a fairer comparison with our completeness corrected LMC mass function.

We note that there are four measurements of Galactic high mass indices which are consistent with our high mass index. Orion B as measured by both [Motte et al. \(2001\)](#) and [Johnstone et al. \(2001\)](#) is consistent within the uncertainties despite values about 20 per cent shallower than ours because the indices have uncertainties of almost 25 per cent. The remaining fields whose high mass indices matches ours, M8 and M17, have large enough differences in analysis that we do not believe they present an issue. The cores from M8 were identified by eye rather than algorithmically as well as being fit with an assumed Gaussian profile unlike most of the other clump finding, including our own. For M17, the mass functions were either fit as well or better by a lognormal form so it may not be a fair comparison with our mass function if it is not well characterized by a double power law.

The break masses from the Milky Way regions are all significantly smaller than the best fit break mass for the LMC. Galactic break masses range from  $0.2 \pm 0.1$  to

$400 \pm 300 M_{\odot}$ . These differences are not surprising as [Reid et al. \(2010\)](#) showed a correlation between distance and break mass using mass functions derived from synthetic observations of a simulated GMC. This trend can even be seen among the 11 mass functions from [Reid & Wilson \(2006b\)](#) as the break masses increase in step with decreasing spatial resolution. Our results for the break mass in the LMC are reasonable given the much greater distance to the clumps.

Fig. 8 shows this comparison in another way. All Milky Way mass functions are reproduced from [Reid & Wilson \(2006b\)](#), while the LMC mass function is scaled such that the lowest mass ( $205 M_{\odot}$ ) is equal to the median maximum Milky Way mass ( $120 M_{\odot}$ ) and the lowest mass has  $N(\geq M) = 1$ . Although this scaling is rather arbitrary, it illustrates the potential connection of the mass function shape between the lower masses in the Milky Way and the higher masses in the LMC.

Other recent observations have also measured the mass function of cores and clumps in the Milky Way. [Netterfield et al. \(2009\)](#) observed 50 square degrees of the Galactic Plane in Vela with the balloon-borne large aperture submillimeter telescope (BLAST) and fit cold cores ( $<14$  K) with a power law of  $-3.22 \pm 0.14$  and warmer cores with an index of  $-1.95 \pm 0.05$ . 738 cores were extracted from Herschel Gould Belt Survey observations of Aquila by [Könyves et al. \(2015\)](#). They fit their mass function with an index of  $-2.33 \pm 0.06$ , but after applying an age correction to the distribution they fit an index of  $-2.0 \pm 0.2$ . [Pattle et al. \(2017\)](#) observed the Cepheus flare region with SCUBA-2 which included four molecular clouds L1147/L1158, L1174, L1251 and L1228. Individual power law fits gave indices of  $-1.8 \pm 0.2$ ,  $-2.0 \pm 0.2$ ,  $-1.8 \pm 0.1$  and  $-2.3 \pm 0.3$ , respectively, while fitting all regions together with a double power law gave a low mass index of  $-1.9 \pm 0.1$  and a high mass index of  $-2.6 \pm 0.3$ . These results are in line with our conclusion that the high

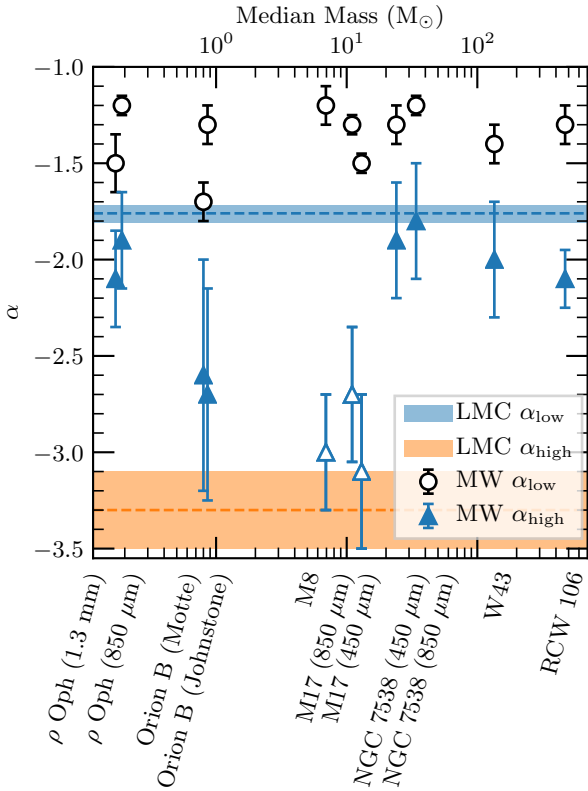


**Figure 7.** Comparison of the double power law mass function fits from the seven Galactic star forming regions summarized in Reid & Wilson (2006b) with the low and high mass fit indices for our LMC mass function. Circles and triangles show the Galactic low and high mass indices, respectively. The orange and blue dashed lines and shaded regions show the low and high mass indices for the LMC, respectively. Milky Way clouds are arranged with their median core/clump masses increasing to the right. Open triangles denote less robust high mass slope determinations for Galactic clouds M8 (clumps identified by eye) and M17 (mass function fit better by lognormal function).

mass Milky Way mass function slope is similar to the low mass LMC slope, except when the entire Cepheus flare region is analyzed together.

Another interesting comparison we can make is to the clump mass function for 30 Dor-10 derived by Indebetouw et al. (2013) using  $^{13}\text{CO}$  (2-1) and  $^{12}\text{CO}$  (2-1) data. Their single power law fit to the differential logarithmic mass distribution of CO clumps above  $500 M_{\odot}$  resulted in a slope of  $\alpha = -1.9 \pm 0.2$  which is consistent with the low mass index measured from dust masses in this work. Fitting the differential form of the mass function resulted in only about five bins, two of which only have one or two clumps, so it is reasonable that the bins below our break mass would dominate their fit. The similar mass range between our dust estimated masses and their independent CO estimated masses is evidence for the accuracy of our dust-only map generation and our estimated dust properties.

Reid & Wilson (2006b) also presented lognormal fits to the Galactic mass functions listed in Fig. 7. The Milky Way values for  $M_0$  are all significantly less than the LMC value with only RCW 106 coming within  $\sim 2\sigma$ , but this is expected

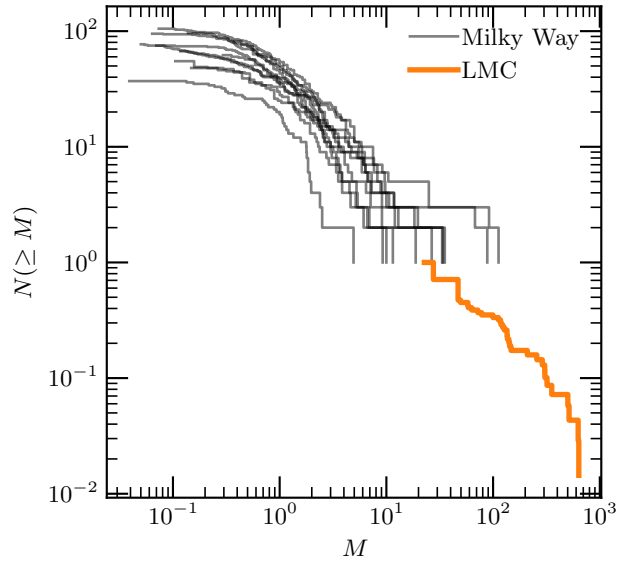


**Figure 8.** All Milky Way mass functions described in Reid & Wilson (2006b) reproduced from their Fig. 8 in gray. The LMC mass function, in orange, has been normalized such that the lowest mass clump is equal to the median of the maximum masses from the Galactic mass functions, and  $N(\geq M)$  normalized such that the lowest mass has  $N(\geq M) = 1$ .

as  $M_0$  is correlated with the mass function median mass like the double power law break mass. We find agreement in the LMC  $\sigma$  value and six of the Galactic mass functions. Both  $\rho$  Oph measurements, M8 and NGC 7538 measured at 850  $\mu\text{m}$  show significantly different best fit values for  $\sigma$ .

We can also search for a link between the LMC clump mass function and the mass distribution of groups of stars as they are first formed. The slope of  $-2$  for young clusters measured by Lada & Lada (2003) is quite similar to our low mass slope over a similar mass range. Analogous to how the similar shape of core mass functions and the stellar IMF has been posited as indicating a constant star formation efficiency, the similarity of the clump and cluster mass functions may result from a constant cluster formation efficiency.

However, dust obscuration challenges observational measurements of the youngest, most deeply embedded star clusters. This hinders our ability to fully constrain the initial mass distribution of clusters as their stars are first born. Cluster formation simulations can bridge the gap between starless molecular clumps and the first star clusters as they emerge from their natal molecular clouds. Fujii & Portegies Zwart (2015) use a hydrodynamical simulation of the parent GMC and after about a free-fall time instantaneously remove the gas and continue a solely N-body simulation of the stars formed. They measure mass function indices of  $-1.73$  at 2 Myr and  $-1.67$  at 10 Myr for a range of initial GMC masses from  $4 \times 10^4$  to  $5 \times 10^6 M_{\odot}$ . Howard et al. (2017) aimed to simulate cluster formation with the inclusion of radiative feedback in their hydrodynamical simulations to study its impact on cluster forming efficiency. Starting from GMCs of similar masses as Fujii & Portegies Zwart (2015) they found close agreement between their simulated mass

function power law index of  $-1.99 \pm 0.14$  and observed embedded clusters. This was after 5 Myr and for masses from 10 to  $2000 M_{\odot}$ . For clusters  $>2000 M_{\odot}$  they fit a steeper power law of  $-3.8$ . These theoretical results are broadly consistent with the LMC clump mass function presented here.

## 5 CONCLUSIONS

We have presented a clump mass function measured in continuum dust emission from star forming molecular clouds in the LMC derived from public archival ALMA observations. 32 clumps were observed in the 30 Dor-10, N159W, and N159E regions with masses ranging between  $205 M_{\odot}$  and  $5740 M_{\odot}$ . To derive these total masses from the thermal dust emission we presented a technique of combining 3.2 and 1.3 mm maps to remove free-free emission contamination and produce dust-only emission maps. We implemented a point source completeness correction to the clump numbers to account for the sensitivity and finite resolution of the observations

From our clump mass function we derived a double power law best fit with parameters  $\alpha_{\text{low}} = -1.76^{+0.04}_{-0.05}$ ,  $\alpha_{\text{high}} = -3.3 \pm 0.2$ , and  $M_{\text{break}} = 2500^{+300}_{-200} M_{\odot}$ . Our low mass power law index is similar to the high mass indices of Milky Way regions hosting lower mass cores and clumps. This may indicate an extension of the Milky Way power law to higher masses. The addition of more clumps from more regions in the LMC along with mass functions derived from spectral line emission will be necessary to better characterize the mass distribution of these objects in the LMC and to investigate its consistency with the Milky Way mass functions.

## ACKNOWLEDGEMENTS

We thank the anonymous referee for detailed comments that improved the content of this paper. This paper makes use of the following ALMA data:

ADS/JAO.ALMA#2011.0.00471.S,  
 ADS/JAO.ALMA#2012.1.00554.S,  
 ADS/JAO.ALMA#2012.1.00603.S,  
 ADS/JAO.ALMA#2013.1.00832.S,  
 ADS/JAO.ALMA#2013.1.01091.S,  
 ADS/JAO.ALMA#2013.1.01136.S, and  
 ADS/JAO.ALMA#2016.1.01533.S.

ALMA is a partnership of ESO (representing its member states), NSF (USA) and NINS (Japan), together with NRC (Canada), MOST and ASIAA (Taiwan), and KASI (Republic of Korea), in cooperation with the Republic of Chile. The Joint ALMA Observatory is operated by ESO, AUI/NRAO and NAOJ. The National Radio Astronomy Observatory is a facility of the National Science Foundation operated under cooperative agreement by Associated Universities, Inc. This research has made use of NASA's Astrophysics Data System Bibliographic Services. This research made use of Astropy, a community-developed core Python package for Astronomy (Astropy Collaboration, 2013). This research made use of APLpy, an open-source plotting package for Python (Robitaille and Bressert, 2012). This research has made use of

the AstroBetter blog and wiki. CDW acknowledges financial support from the Canada Council for the Arts through a Killam Research Fellowship. The research of CDW is supported by grants from the Natural Sciences and Engineering Research Council of Canada and the Canada Research Chairs program.

## REFERENCES

- Adams F. C., Fatuzzo M., 1996, *ApJ*, **464**, 256  
 Alves J., Lombardi M., Lada C. J., 2007, *A&A*, **462**, L17  
 Alves J., Lombardi M., Lada C. J., 2017, *A&A*, **606**, L2  
 André P., et al., 2010, *A&A*, **518**, L102  
 Arzoumanian D., et al., 2011, *A&A*, **529**, L6  
 Ballesteros-Paredes J., Vázquez-Semadeni E., Gazol A., Hartmann L. W., Heitsch F., Colín P., 2011, *MNRAS*, **416**, 1436  
 Berry D. S., Reinhold K., Jenness T., Economou F., 2007, in Shaw R. A., Hill F., Bell D. J., eds, *Astronomical Society of the Pacific Conference Series Vol. 376, Astronomical Data Analysis Software and Systems XVI*. p. 425  
 Bica E., Claria J. J., Dottori H., 1992, *AJ*, **103**, 1859  
 Bolatto A. D., Jackson J. M., Israel F. P., Zhang X., Kim S., 2000, *ApJ*, **545**, 234  
 Briggs D. S., 1995, in *American Astronomical Society Meeting Abstracts*. p. 1444  
 Bromm V., 2005, in Corbelli E., Palla F., Zinnecker H., eds, *Astrophysics and Space Science Library Vol. 327, The Initial Mass Function 50 Years Later*. p. 469, doi:10.1007/978-1-4020-3407-7\_85  
 Chabrier G., 2003, *PASP*, **115**, 763  
 Chabrier G., 2005, in Corbelli E., Palla F., Zinnecker H., eds, *Astrophysics and Space Science Library Vol. 327, The Initial Mass Function 50 Years Later*. p. 41 (arXiv:astro-ph/0409465), doi:10.1007/978-1-4020-3407-7\_5  
 Chabrier G., Hennebelle P., 2010, *ApJ*, **725**, L79  
 Currie M. J., Berry D. S., Jenness T., Gibb A. G., Bell G. S., Draper P. W., 2014, in Manset N., Forshay P., eds, *Astronomical Society of the Pacific Conference Series Vol. 485, Astronomical Data Analysis Software and Systems XXIII*. p. 391  
 De Becker M., Rauq F., 2013, *A&A*, **558**, A28  
 De Marchi G., et al., 2011, *ApJ*, **739**, 27  
 Dufour R. J., 1984, in van den Bergh S., de Boer K. S. D., eds, *IAU Symposium Vol. 108, Structure and Evolution of the Magellanic Clouds*. pp 353–360  
 Fall S. M., Chandar R., 2012, *ApJ*, **752**, 96  
 Freeman P., Rosolowsky E., Kruijssen J. M. D., Bastian N., Adamo A., 2017, *MNRAS*, **468**, 1769  
 Fujii M. S., Portegies Zwart S., 2015, *MNRAS*, **449**, 726  
 Fujii K., et al., 2014, *ApJ*, **796**, 123  
 Fukui Y., et al., 1999, *PASJ*, **51**, 745  
 Fukui Y., Mizuno N., Yamaguchi R., Mizuno A., Onishi T., 2001, *PASJ*, **53**, L41  
 Fukui Y., et al., 2008, *ApJS*, **178**, 56  
 Fukui Y., et al., 2015, *ApJ*, **807**, L4  
 Ginsburg A., et al., 2016, *A&A*, **595**, A27  
 Gordon K. D., et al., 2014, *ApJ*, **797**, 85  
 Guszejnov D., Hopkins P. F., 2015, *MNRAS*, **450**, 4137  
 Harris W. E., Blakeslee J. P., Whitmore B. C., Gnedin O. Y., Geisler D., Rothberg B., 2016, *ApJ*, **817**, 58  
 Heikkilä A., Johansson L. E. B., Olofsson H., 1998, *A&A*, **332**, 493  
 Heikkilä A., Johansson L. E. B., Olofsson H., 1999, *A&A*, **344**, 817  
 Henize K. G., 1956, *ApJS*, **2**, 315

Howard C. S., Pudritz R. E., Harris W. E., 2017, *MNRAS*, **470**, 3346

Hughes A., et al., 2010, *MNRAS*, **406**, 2065

Imai H., Katayama Y., Ellingsen S. P., Hagiwara Y., 2013, *MNRAS*, **432**, L16

Indebetouw R., Johnson K. E., Conti P., 2004, *AJ*, **128**, 2206

Indebetouw R., et al., 2013, *ApJ*, **774**, 73

Johansson L. E. B., Olofsson H., Hjalmarson A., Gredel R., Black J. H., 1994, *A&A*, **291**, 89

Johansson L. E. B., et al., 1998, *A&A*, **331**, 857

Johnstone D., Fich M., Mitchell G. F., Moriarty-Schieven G., 2001, *ApJ*, **559**, 307

Kawamura A., et al., 2009, *ApJS*, **184**, 1

Könyves V., et al., 2015, *A&A*, **584**, A91

Krumholz M. R., 2014, *Phys. Rep.*, **539**, 49

Lada E. A., 1992, *ApJ*, **393**, L25

Lada C. J., Lada E. A., 2003, *ARA&A*, **41**, 57

Lada E. A., Bally J., Stark A. A., 1991a, *ApJ*, **368**, 432

Lada E. A., Depoy D. L., Evans II N. J., Gatley I., 1991b, *ApJ*, **371**, 171

Larson R. B., 1973, *MNRAS*, **161**, 133

Lazendic J. S., Dickel J. R., Jones P. A., 2003, *ApJ*, **596**, 287

McMullin J. P., Waters B., Schiebel D., Young W., Golap K., 2007, in Shaw R. A., Hill F., Bell D. J., eds, *Astronomical Society of the Pacific Conference Series Vol. 376*, *Astronomical Data Analysis Software and Systems XVI*. p. 127

Meixner M., et al., 2006, *AJ*, **132**, 2268

Meixner M., et al., 2013, *AJ*, **146**, 62

Mizuno N., Rubio M., Mizuno A., Yamaguchi R., Onishi T., Fukui Y., 2001, *PASJ*, **53**, L45

Mizuno Y., et al., 2010, *PASJ*, **62**, 51

More J., 1977, Levenberg-Marquardt algorithm: implementation and theory. <http://www.osti.gov/scitech/servlets/purl/7256021>

Motte F., André P., Ward-Thompson D., Bontemps S., 2001, *A&A*, **372**, L41

Netterfield C. B., et al., 2009, *ApJ*, **707**, 1824

Padoan P., Nordlund A., Jones B. J. T., 1997, *MNRAS*, **288**, 145

Paron S., Ortega M. E., Cunningham M., Jones P. A., Rubio M., Fariña C., Komugi S., 2014, *A&A*, **572**, A56

Paron S., Ortega M. E., Fariña C., Cunningham M., Jones P. A., Rubio M., 2016, *MNRAS*, **455**, 518

Pattle K., et al., 2017, *MNRAS*, **464**, 4255

Pietrzyński G., et al., 2013, *Nature*, **495**, 76

Planck Collaboration et al., 2016, *A&A*, **594**, A28

Reid M. A., Wilson C. D., 2005, *ApJ*, **625**, 891

Reid M. A., Wilson C. D., 2006a, *ApJ*, **644**, 990

Reid M. A., Wilson C. D., 2006b, *ApJ*, **650**, 970

Reid M. A., Wadsley J., Petitclerc N., Sills A., 2010, *ApJ*, **719**, 561

Rolleston W. R. J., Trundle C., Dufton P. L., 2002, *A&A*, **396**, 53

Roman-Duval J., Bot C., Chastenet J., Gordon K., 2017, *ApJ*, **841**, 72

Rubio M., Elmegreen B. G., Hunter D. A., Brinks E., Cortés J. R., Cigan P., 2015, *Nature*, **525**, 218

Saigo K., et al., 2017, *ApJ*, **835**, 108

Salpeter E. E., 1955, *ApJ*, **121**, 161

Schruba A., et al., 2017, *ApJ*, **835**, 278

Seale J. P., Looney L. W., Wong T., Ott J., Klein U., Pineda J. L., 2012, *ApJ*, **751**, 42

Selman F. J., Melnick J., 2013, *A&A*, **552**, A94

Staveley-Smith L., Kim S., Calabretta M. R., Haynes R. F., Kesteven M. J., 2003, *MNRAS*, **339**, 87

Tassis K., Christie D. A., Urban A., Pineda J. L., Mouschovias T. C., Yorke H. W., Martel H., 2010, *MNRAS*, **408**, 1089

Turner J. L., Ho P. T. P., Beck S. C., 1998, *AJ*, **116**, 1212

Walborn N. R., Blades J. C., 1987, *ApJ*, **323**, L65

Ward J. L., Oliveira J. M., van Loon J. T., Sewilo M., 2016, *MNRAS*, **455**, 2345

Williams J. P., de Geus E. J., Blitz L., 1994, *ApJ*, **428**, 693

Wong T., et al., 2011, *ApJS*, **197**, 16

Wong T., et al., 2017, *ApJ*, **850**, 139

Wood D. O. S., Churchwell E., 1989, *ApJS*, **69**, 831

## APPENDIX A: OBSERVED, DUST-ONLY, AND FREE-FREE-ONLY MAPS

Here we present maps for 30 Dor-10, N159W, and N159E as observed and also the dust-only and free-free-only emission estimated from our algebraic combination in both Bands 3 and 6. Equation 6 was used to produce the dust-only maps in Band 6. Free-free-only emission maps in Band 6 were made using Equations 4 and 5 to solve for the expression

$$S_{\text{ff}} = \frac{S_{\text{B3}} - S_{\text{B6}} \left( \frac{\nu_{\text{B3}}}{\nu_{\text{B6}}} \right)^{(2+\beta)}}{\left( \frac{\nu_{\text{B3}}}{\nu_{\text{B6}}} \right)^{-0.1} - \left( \frac{\nu_{\text{B3}}}{\nu_{\text{B6}}} \right)^{(2+\beta)}}. \quad (\text{A1})$$

Dust-only and free-free-only emission maps in Band 3 were created by starting instead from

$$S_{\text{B3}} = S_{\text{d}} + S_{\text{ff}} \quad (\text{A2})$$

and

$$S_{\text{B6}} = S_{\text{d}} \left( \frac{\nu_{\text{B6}}}{\nu_{\text{B3}}} \right)^{(2+\beta)} + S_{\text{ff}} \left( \frac{\nu_{\text{B6}}}{\nu_{\text{B3}}} \right)^{-0.1} \quad (\text{A3})$$

where  $S_{\text{d}}$  and  $S_{\text{ff}}$  are now the dust-only and free-free-only flux densities at 3.2 mm. We used these to solve for the expressions

$$S_{\text{d}} = S_{\text{B3}} - \frac{S_{\text{B6}} - S_{\text{B3}} \left( \frac{\nu_{\text{B6}}}{\nu_{\text{B3}}} \right)^{(2+\beta)}}{\left( \frac{\nu_{\text{B6}}}{\nu_{\text{B3}}} \right)^{-0.1} - \left( \frac{\nu_{\text{B6}}}{\nu_{\text{B3}}} \right)^{(2+\beta)}} \quad (\text{A4})$$

and

$$S_{\text{ff}} = \frac{S_{\text{B6}} - S_{\text{B3}} \left( \frac{\nu_{\text{B6}}}{\nu_{\text{B3}}} \right)^{(2+\beta)}}{\left( \frac{\nu_{\text{B6}}}{\nu_{\text{B3}}} \right)^{-0.1} - \left( \frac{\nu_{\text{B6}}}{\nu_{\text{B3}}} \right)^{(2+\beta)}}. \quad (\text{A5})$$

Figures A1 through A3 show all maps produced for 30 Dor-10, N159W, and N159E in this work. The top rows show the observed maps, the middle rows the free-free-only emission maps, and the bottom rows the dust-only emission maps. Left columns are maps in Band 3 and right columns are maps in Band 6. All maps are presented with the same spatial and color axes scaling and ranges to facilitate comparisons between the morphologies of the different bands and emission sources.

30 Dor-10 exhibits its strongest emission in Band 6 with compact dust sources accounting for most of the flux. N159W and N159E show similar levels of emission in both bands, due to most of the light coming from free-free emission, which slowly varies with frequency. All three fields show the gradual change in free-free brightness between Bands 3 and 6 and the much stronger drop in the dust emission when going from higher to lower frequencies.

This paper has been typeset from a  $\text{\TeX}/\text{\LaTeX}$  file prepared by the author.

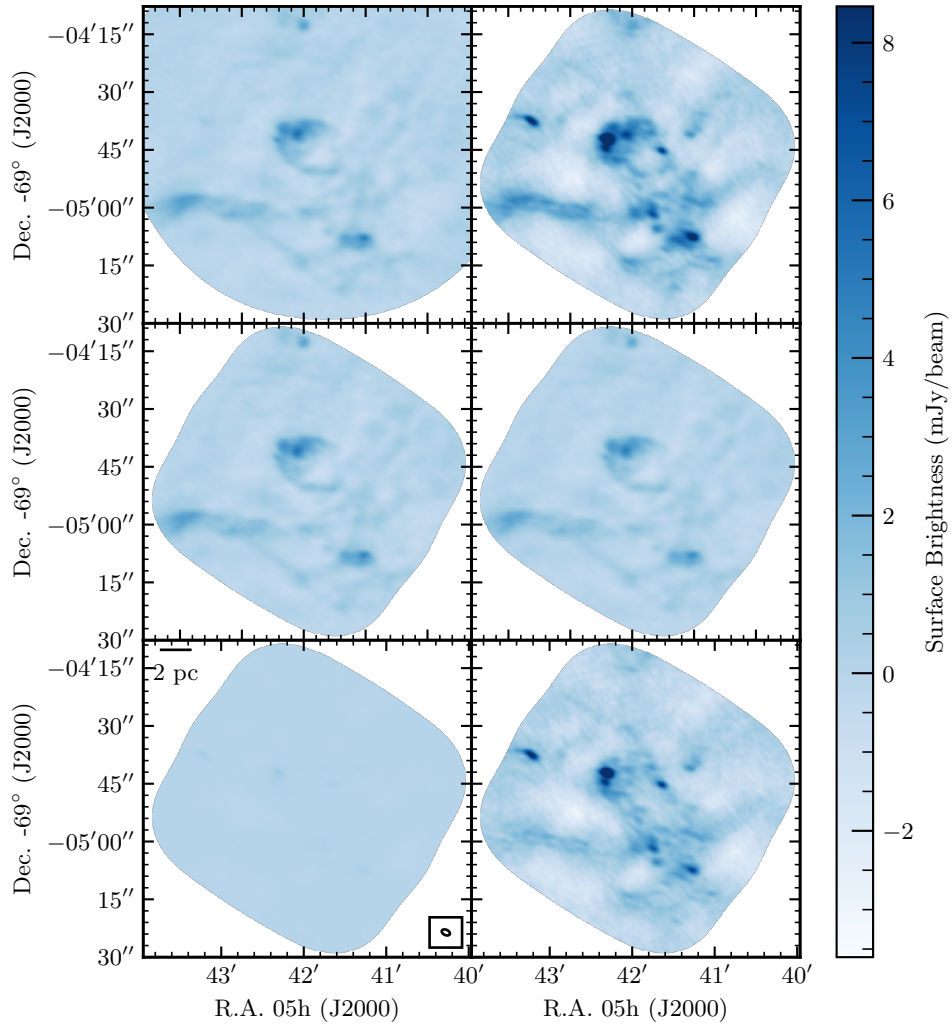


**Figure A1.** Maps of 30 Dor-10 in 3.2 mm (left column) and 1.3 mm (right column) continuum along with maps of free-free-only (middle row) and dust-only (bottom row) emission at both wavelengths. Spatial and color coordinate axes are matched between each map. The uv coverage of each map has been matched and the synthesized beam shape is represented by the ellipse in the bottom-left panel.



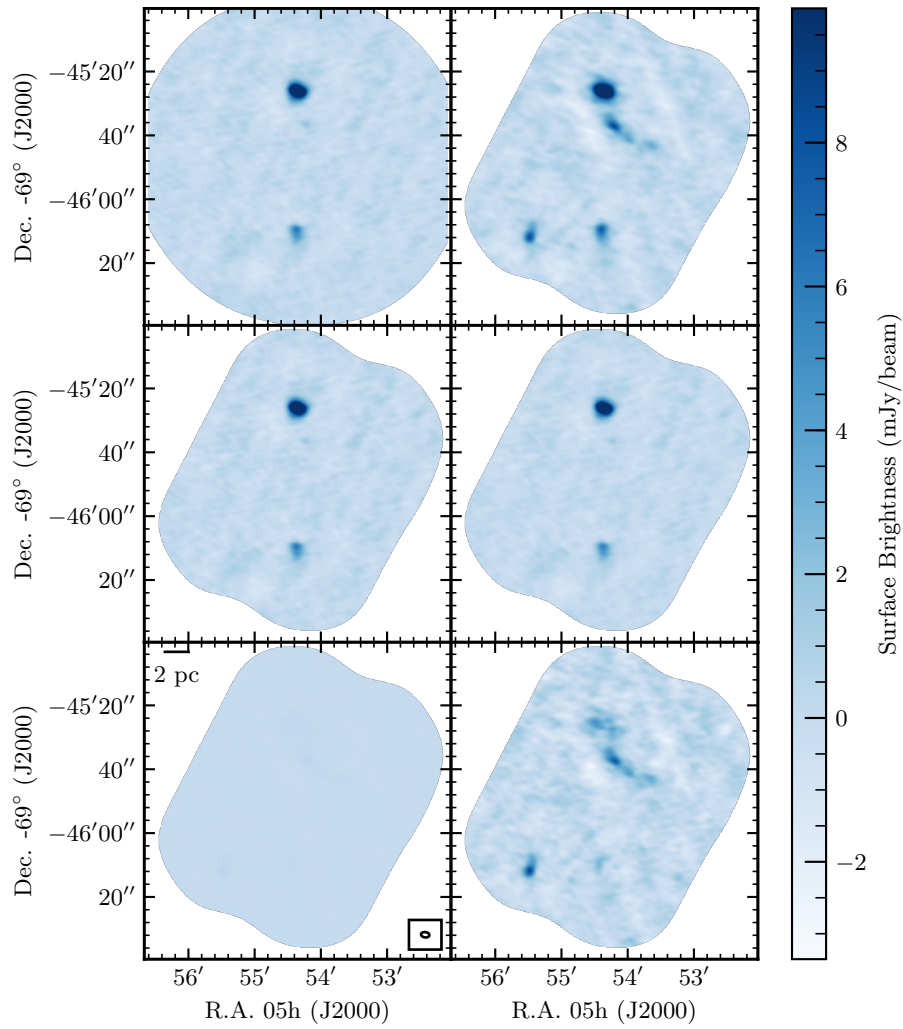


**Figure A2.** Same as Figure A1 but showing N159W observations.

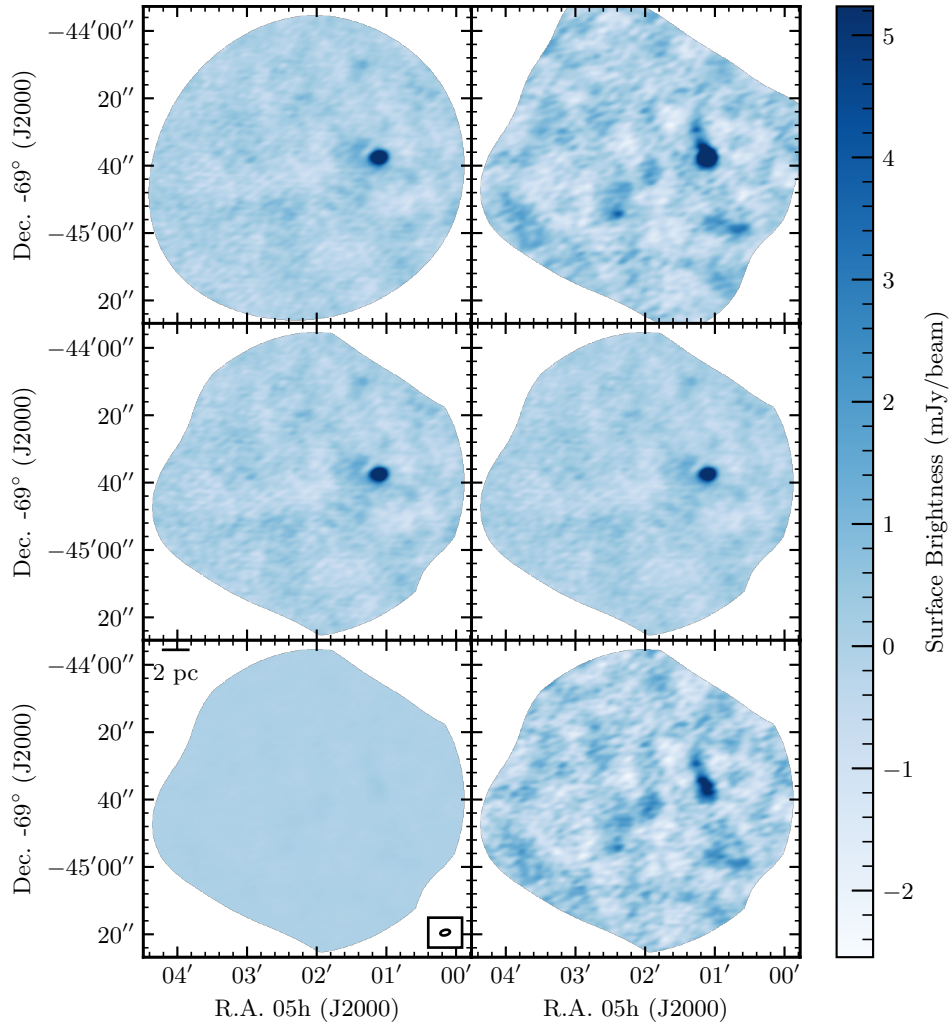


**Figure A3.** Same as Figure A1 but showing N159E observations.